

## Cumulant Green's function calculations of plasmon satellites in bulk sodium: Influence of screening and the crystal environment

Jianqiang Sky Zhou,<sup>1,2,\*</sup> Matteo Gatti,<sup>1,2,3</sup> J. J. Kas,<sup>2,4</sup> J. J. Rehr,<sup>2,4</sup> and Lucia Reining<sup>1,2</sup>

<sup>1</sup>Laboratoire des Solides Irradiés, École Polytechnique, CNRS, CEA, Université Paris-Saclay, F-91128 Palaiseau, France

<sup>2</sup>European Theoretical Spectroscopy Facility (ETSF)

<sup>3</sup>Synchrotron SOLEIL, L'Orme des Merisiers, Saint-Aubin, BP 48, F-91192 Gif-sur-Yvette, France

<sup>4</sup>Department of Physics, University of Washington, Seattle, Washington 98195-1560, USA



(Received 4 August 2017; revised manuscript received 14 November 2017; published 16 January 2018)

We present *ab initio* calculations of the photoemission spectra of bulk sodium using different flavors of the cumulant expansion approximation for the Green's function. In particular, we study the dispersion and intensity of the plasmon satellites. We show that the satellite spectrum is much more sensitive to many details than the quasiparticle spectrum, which suggests that the experimental investigation of satellites could yield additional information beyond the usual studies of the band structure. In particular, a comparison to the homogeneous electron gas shows that the satellites are influenced by the crystal environment, although the crystal potential in sodium is weak. Moreover, the temperature dependence of the lattice constant is reflected in the position of the satellites. Details of the screening also play an important role; in particular, the contribution of transitions from  $2s$  and  $2p$  semicore levels influences the satellites, but not the quasiparticle. Moreover, inclusion of contributions to the screening beyond the random-phase approximation has an effect on the satellites. Finally, we elucidate the importance of the coupling of electrons and holes by comparing the results of the time-ordered and the retarded cumulant expansion approximations. Again, we find small but noticeable differences. Since all the small effects add up, our most advanced calculation yields a satellite position which is improved with respect to previous calculations by almost 1 eV. This stresses the fact that the calculation of satellites is much more delicate than the calculation of a quasiparticle band structure.

DOI: [10.1103/PhysRevB.97.035137](https://doi.org/10.1103/PhysRevB.97.035137)

### I. INTRODUCTION

Photoemission spectroscopy has proved increasingly useful in the elucidation of the electronic properties of materials, since it provides both quasiparticle band structures, with information of one-particle-like excitations, and satellite structures that reflect the coupling to bosonic excitations such as phonons, plasmons, and magnons [1]. Accurate descriptions of photoemission spectra from *ab initio* calculations have been a challenge for ages.

Currently, the most widely used approach for moderately correlated materials is the *GW* approximation (GWA) proposed by Hedin in 1965 [2]. In the GWA, the one-particle Green's function is determined by a Dyson equation  $G = G_H + G_H \Sigma_{xc} G$ , where  $G_H$  is the Hartree Green's function, and  $\Sigma_{xc}$  is a complex, nonlocal, and frequency-dependent self-energy that is approximated as a convolution of the one-particle Green's function  $G$  and the dynamically screened Coulomb interaction  $W$ , leading to  $\Sigma_{xc} = GW$ . The GWA has become the state-of-the-art approach to compute quasiparticle band structures. However, one of its notable shortcomings is the poor description of the satellite structures in photoemission spectra [3]. Since plasmons are the dominant structures in the inverse dielectric function  $\epsilon^{-1}$  and hence in  $W = \epsilon^{-1}v_c$ , where  $v_c$  is the bare Coulomb interaction, one might suppose that plasmon satellites should be well described by the GWA. However, this

is not the case in practice. An example is the spurious prediction of a sharp plasmaron satellite, which has been contradicted experimentally [4–7]. Moreover, the GWA satellites due to plasmons are generally too far from the quasiparticle energy compared to experiment [6–12].

Alternatively, the cumulant expansion approximation (CEA) has been quite promising for giving a better description of plasmon satellites in photoemission spectra in a number of systems [6–20]. The CEA was inspired by the exact Green's function of an electron-boson model Hamiltonian for a core level [21] and has been hence extensively used for core-level photoemission (see, e.g., [22–25]), and also in other contexts, such as for the electron-phonon interaction and the polaron problem (see, e.g., [26–30]), or for modeling ultrafast electron dynamics (see, e.g., [31–33]). The CEA extrapolates the exact cumulant average of the evolution operator [34] to obtain an approximate exponential representation of the Green's function in the time domain  $G(t) = G_H(t)e^{C(t)}$ , the expansion of which yields a Poisson series of satellites in the spectral function  $A(\omega) = \pi^{-1}|\text{Im} G(\omega)|$ , consistent with experimental observations. Moreover, to lowest order in the screened interaction the cumulant function  $C(t)$  can be expressed in terms of the *GW* self-energy, and it is therefore computationally no more demanding than the GWA itself.

The number of *ab initio* CEA calculations to date is still relatively limited. Therefore, many details remain to be understood and settled. First, better agreement of CEA results with experiment is expected in insulators, semiconductors, or core levels of metals than in metal valence bands [16]. The reason

\*jianqiang.zhou@polytechnique.edu

is that the traditional time-ordered cumulant (TOC) is exact only in the limit of an approximate core-level Hamiltonian [21] or for an approximation that decouples different orbitals [6,16]. Both of these approximations assume that at zero temperature the occupation numbers are either 0 or 1, which is certainly not true close to the Fermi level of metals. A number of efforts have been made in order to go beyond the TOC to describe systems with partially occupied states. For example, the retarded cumulant (RC) approximation was recently proposed [35,36], where both the Green's function and the self-energy appearing in the CEA are replaced by their retarded counterparts. Consequently, while within the TOC unoccupied states do not produce satellites below the Fermi level, these additional features, which are a signature of coupling between occupied and unoccupied states, have been obtained in the homogeneous electron gas by using the RC [35]. Second, as pointed out above, the calculations rely on a GWA self-energy, which has been extensively studied for calculations of quasiparticle band structures. However, the insight gained from these studies is not necessarily transferable to the satellites, which are considerably enhanced by the CEA with respect to the GWA calculation. Indeed, our work shows that several effects influence the satellites, whereas they can be often overlooked for the quasiparticles. These include mild changes in the crystal environment and the lattice constant, the contribution of core levels, and the approximation used for the screening.

We illustrate these points by performing both TOC and RC calculations for the valence photoemission spectrum of bulk sodium. Our most detailed calculation, which takes into account all the aspects mentioned above, leads to an improvement of the satellite position of almost 1 eV with respect to previous calculations [16], as compared to experiment [37].

This paper starts in Sec. II with a brief introduction to the theoretical framework, where those aspects are highlighted that are important for the subsequent analysis. In Sec. III the results of the time-ordered and the retarded CEA are compared. Section IV discusses the effects of the crystal environment and the semicore transitions on the spectra. Section V deals with the approximations used to calculate the screening. In Sec. VI we compare our result to experiment. Finally, Sec. VII contains the conclusions. Computational details are relegated to the Appendix.

## II. THEORETICAL FRAMEWORK

In this section we summarize the main theoretical ingredients. The purpose of the section is to highlight the ideas behind the existing cumulant approximations, to explain in which way they constitute an improvement with respect to the GWA, and what is the difference between various cumulant flavors. It is a summary section referring to previous work in the literature.

The subject of interest here is the diagonal elements of the one-body Green's function at equilibrium at zero temperature. It describes electron addition and removal to a many-body system, expressed in terms of the greater ( $>$ ) and lesser ( $<$ ) components:

$$\begin{aligned} G_k^>(\tau) &= -i \langle N | c_k(\tau) c_k^\dagger(0) | N \rangle, \\ G_k^<(\tau) &= +i \langle N | c_k^\dagger(0) c_k(\tau) | N \rangle, \end{aligned} \quad (1)$$

where we have defined the creation and annihilation operators  $c_k^\dagger$  and  $c_k$ , respectively, for an electron in a state with quantum number  $k$  (note that in a crystal  $k$  stands in general for a band  $n$  and a  $\mathbf{k}$  point), which act on the ground-state  $|N\rangle$  of  $N$  interacting electrons.

These components can be combined in various ways, which are equivalent if observables are calculated consistently. In particular, the *time-ordered* Green's function reads

$$G_k^T(\tau) = \theta(\tau) G_k^>(\tau) + \theta(-\tau) G_k^<(\tau) \quad (2)$$

and the *retarded* Green's function is

$$G_k^R(\tau) = \theta(\tau) [G_k^>(\tau) - G_k^<(\tau)]. \quad (3)$$

In both cases, the diagonal elements of the spectral function can be calculated as

$$\begin{aligned} A_k(\omega) &= \frac{i}{2\pi} [G_k^>(\omega) - G_k^<(\omega)] \\ &= \frac{1}{\pi} |\text{Im} G_k^T(\omega)| = -\frac{1}{\pi} \text{Im} G_k^R(\omega). \end{aligned} \quad (4)$$

For a not too strongly correlated material  $A_k(\omega)$  contains in general a quasiparticle (QP) peak, which is a broadened and shifted reminder of the single-particle peak in the noninteracting spectrum, and satellites, which are additional structures to which weight is transferred from the quasiparticle peak. The latter has therefore less weight than in the noninteracting case. The quasiparticles constitute the band structure in a solid.

Often, the Green's function is calculated from the Dyson equation, which is an integral equation whose kernel is the self-energy. Today the state-of-the-art approach for band structure calculations is the *GW* approximation for the self-energy. However, it has been known for a long time that satellites in the spectral function are less well described by the GWA than quasiparticle energies. This emerges most clearly when one considers simple models, such as a Hamiltonian consisting of a single fermionic level coupled to bosons. In our case, the boson represents a dominant excitation in the dynamically screened Coulomb interaction  $W$ . The model was solved exactly by Langreth in 1970 [21]. He found that the exact spectral function consists of one QP peak followed by a Poisson series of boson replicas. The corresponding Green's function  $G(\tau)$  can be written as the noninteracting Green's function  $G_0(\tau)$  multiplied by an exponential  $e^{C(\tau)}$ , where  $C$  is the cumulant that contains the bosons. The GWA, on the other side, yields a good description of the QP energy but a poor satellite spectrum. Indeed, the GWA corresponds in the model to a second-order expansion of the self-energy in the coupling constant  $g$ . As a consequence, quantities such as the QP renormalization are correct to first order in  $g^2$ , but just one satellite appears, which can be interpreted as an average representing the whole satellite series of the exact spectrum [38].

The simple model of a single fermion level is reasonable to represent deep core states and, indeed, core-level photoemission spectra are often well described by a spectral function of the exponential (cumulant) form. When one goes beyond isolated levels, the picture of independent quasiparticles coupled to bosons remains often reasonable. Also for a two-level model a cumulant Green's function is a much better approximation to the exact solution than the GWA [39], in a wide parameter range. For the general case and real materials, approximate

cumulant Green's functions have been derived in various ways, based for example on diagrammatic arguments [30,39–41], on the equation of motion for the one-body Green's function [42], on the Kadanoff-Baym equations [6], or starting from the Dyson equation and imposing a cumulant form on the Green's function [8]. In all cumulant approximations, greater and lesser components of the Green's function are of the form

$$G_k^{<>}(\tau) \propto e^{-i\varepsilon_k\tau} e^{C_k^{<>}(\tau)}, \quad (5)$$

where  $\varepsilon_k$  is a quasiparticle energy for a state  $k$ . The rationale underlying this exponential ansatz for diagonal Green's function is that it becomes exact if the vertices of quasiparticle interaction with the heat-bath excitations (i.e., with other quasiparticles) are constrained to the propagation interval  $(0, \tau)$ , likewise in the core-hole problem [21,40]. The cumulant  $C_k$  contains the quasiparticle renormalization and the seed for the satellites that appear when the exponential is expanded. The difference between various cumulant flavors appears in the details of the ingredients. Since beyond the model of an isolated level approximations have to be made, these differences are linked to the coupling between levels, and in particular, to the coupling between occupied and empty states, which is treated differently in different derivations.

The easiest way to illustrate this is to follow the derivations of [8] and the subsequent [35]: These derivations are based on the ansatz (5), and the cumulant is found by imposing that the Green's function should be exact to first order in  $W$ . The differences appear in the details of the ansatz.

In the case of Ref. [8], for an occupied state  $k$  the Green's function reads

$$G_k^{\text{loc}}(\tau) = i\theta(-\tau)e^{-i\varepsilon_k\tau} e^{C_k(\tau)}. \quad (6)$$

In this ansatz only occupied single-particle states contribute to the electron removal spectrum; similarly, the electron addition spectrum is built with unoccupied states only. In other words,  $G_k^> = 0$  when  $k < k_F$ . In Ref. [35] the cumulant form was postulated for the *retarded* Green's function, namely

$$G_k^{\text{rc}}(\tau) = -i\theta(\tau)e^{-i\varepsilon_k\tau} e^{C_k^{\text{rc}}(\tau)}. \quad (7)$$

In this case, occupied and empty states  $k$  can contribute to both electron addition and removal.

In both cases, the unknown  $C_k(\tau)$  is found by constraining the Green's function to the ansatz and by determining the unknown cumulant function to first order in  $W$  from the Dyson equation. The main ingredient that appears in the resulting expressions is the  $GW$  self-energy, since it is of first order in  $W$ . This leads to the fact that in all cases a  $GW$  quasiparticle energy results, and the method is in general referred to as the  $GW+C$  method. In the case of Ref. [8] the Dyson equation in its time-ordered version was used, whereas the Dyson equation for the retarded Green's function appears in Ref. [35]. At zero temperature both versions are of course in principle exact and fully equivalent, but the different approximations in the ansatz lead to a different final result.

In the time-ordered case the occupied and empty spaces are decoupled. There are minor variations due to different points where this decoupling is done; here we concentrate on the TOC of Refs. [6,16] where the cumulant for an occupied

state is

$$C_k(\tau) = \frac{1}{\pi} \int_{-\infty}^{\mu-\varepsilon_k} d\omega |\text{Im} \Sigma_{k,xc}(\omega + \varepsilon_k)| \frac{e^{-i\omega\tau} - 1}{\omega^2}, \quad (8)$$

which is to be used in (6). The analogous TOC for an unoccupied state can be found in [13,14]. The self-energy  $\Sigma_{k,xc}$  is calculated in a  $G_0W_0$  scheme [18], where  $W_0$  is obtained using Kohn-Sham ingredients and  $G_0$  is a quasiparticle (mean-field) choice that is optimized [38,43,44] in an energy-self-consistent scheme in such a way that the quasiparticle energy  $\varepsilon_k$  is equal to  $\varepsilon_{k,H} + \text{Re} \Sigma_{k,xc}(\varepsilon_k)$ , with  $\varepsilon_{k,H}$  the Hartree part. Note that for hole states  $\varepsilon_k$  is smaller than the Fermi energy  $\mu$ .

The cumulant (8) creates satellites in the spectral function for an occupied state  $k$  only on the removal side,  $\omega < \varepsilon_k$ . Similarly, satellites for an unoccupied state are found only in the addition sector. This is perfectly justified for the deep core levels that are indeed decoupled from the high-lying empty states, but it is questionable when one approaches the Fermi surface.

Indeed, near the Fermi surface the spectral function should be more and more symmetric, which means that for  $k \approx k_F$  satellites of similar weight should be found both in the addition and in the removal sectors. This can by definition not be achieved by the ansatz (6). The RC ansatz (7), instead, treats occupied and empty states on the same footing. Therefore the symmetry is restored and one may expect that the RC ansatz is more suitable close to the Fermi surface.

By requiring that the first-order expansion of the retarded Dyson equation and of the RC ansatz be the same, the RC cumulant becomes [35]

$$C_k^{\text{rc}}(\tau) = \frac{1}{\pi} \int_{-\infty}^{\infty} d\omega |\text{Im} \Sigma_{k,xc}^{\text{rc}}(\omega + \varepsilon_k)| \frac{e^{-i\omega\tau} - 1}{\omega^2}. \quad (9)$$

Comparison with Eq. (8) shows that the difference in the cumulant functions is the frequency integration range: the TOC only integrates the hole part of the self-energy (i.e., corresponding to  $\omega < \mu$ ), whereas the RC integrates both hole and electron parts.

Both the TOC and the RC are exact in the case of an isolated level coupled to bosons. Beyond this, both are approximations, based on (i) a linear response approximation which identifies the boson with the screened Coulomb interaction  $W$ ; (ii) an ansatz, or the choice of diagrams of lowest order in  $W$  for the cumulant [21] such that the Green's function is of the form (5); and (iii) the hypothesis that one can concentrate on diagonal elements only, and in particular, that the  $GW$  self-energy is diagonal in the basis of single-particle states. The justification for these approximations is a combination of rigorous mathematical derivations, physical intuition (such as a choice of diagrams, or the electron-boson picture itself), and experience (which supports for example the diagonal approximation of the self-energy). However, it is notoriously difficult to treat the coupling of addition and removal spaces beyond the GWA in a systematic and physically meaningful way (see, e.g., [18,39,45]), and the approximations have still to be judged by their results, both for models and real materials.

In order to illustrate the physical meaning of the different terms in the cumulant function (8), we consider a simple

electron-boson model time-ordered self-energy [39]:

$$\Sigma^{md}(\omega) = \frac{g_1^2/2}{\omega - \varepsilon_1 + \omega_p - i\eta} + \frac{g_2^2/2}{\omega - \varepsilon_2 - \omega_p + i\eta}, \quad (10)$$

where  $g_1$  and  $g_2$  denote the electron-plasmon coupling constant at each orbital,  $\omega_p$  is a nondispersing plasmon energy,  $\varepsilon_1 < \mu$  and  $\varepsilon_2 > \mu$  are the energies of two electronic orbitals representing hole and electron state, respectively, and  $\eta \rightarrow 0^+$  is an infinitesimal positive number. The imaginary part  $\text{Im } \Sigma^{md} = (\pi/2)[g_1^2\delta(\omega - \varepsilon_1 + \omega_p) - g_2^2\delta(\omega - \varepsilon_2 - \omega_p)]$  contains one  $\delta$  peak at  $\omega = \varepsilon_1 - \omega_p$  with weight  $g_1^2/2$  and another one at  $\omega = \varepsilon_2 + \omega_p$  with weight  $g_2^2/2$ .

Using this model self-energy for the TOC cumulant function (8), we have

$$C(\tau) = \frac{g_1^2}{2\omega_p^2} e^{i\omega_p\tau} - \frac{g_1^2}{2\omega_p^2}. \quad (11)$$

The physical meaning of each term in  $C(\tau)$  becomes clear in Eq. (6): the first term generates a series of plasmon satellites at energies  $\omega_p$  away from the quasiparticle energy  $\varepsilon^{\text{loc}}$ . The second term gives the quasiparticle renormalization factor  $Z^{\text{loc}} = \exp\{-g_1^2/(2\omega_p^2)\}$ , which measures the spectral weight corresponding to the quasiparticle excitation, whereas  $(1 - Z^{\text{loc}})$  goes into the rest of the spectral function, including satellites.

When  $\Sigma^{md}$  is instead used in the  $C^R$  (9), we have for the matrix element of  $G$  in the hole state with energy  $\varepsilon_1$

$$C^R(\tau) = \frac{g_1^2}{2\omega_p^2} e^{i\omega_p\tau} + \frac{g_2^2}{2\tilde{\omega}_p^2} e^{-i\tilde{\omega}_p\tau} - \frac{g_1^2}{2\omega_p^2} - \frac{g_2^2}{2\tilde{\omega}_p^2}, \quad (12)$$

where  $\tilde{\omega}_p = \omega_p + \Delta$ , and  $\Delta = \varepsilon_2 - \varepsilon_1$  the quasiparticle energy difference between the two orbitals.

Two more terms appear in  $C^R$  with respect to the time-ordered  $C$  due to the electron part of  $\Sigma^{md}$ . The first new term generates a series of plasmon satellites at energies equal to  $\tilde{\omega}_p$  away from the quasiparticle energy  $\varepsilon_1$ . Due to the minus sign in the exponential, these satellites are placed on the high-energy side of  $\varepsilon_1$ . Therefore, the RC has satellites on both sides of the quasiparticle peak in the spectral function. The second new term modifies the quasiparticle renormalization factor, such that  $Z'^c = \exp\{-g_1^2/(2\omega_p^2) - g_2^2/(2\tilde{\omega}_p^2)\}$ .

Analogously, the RC spectral function of the electron state (i.e., orbital with quasiparticle energy  $\varepsilon_2$ ) also contains satellites with energy below the Fermi energy. As a consequence, in order to have the complete RC electron removal spectrum, one also has to sum the spectral functions of the partially occupied electron states.

For the two-level electron-boson coupling model [39] the TOC and RC results can be compared to the exact ones. As shown in [46], the RC is clearly superior in the parameter range of interest here. Of course, the model is a very rough simplification with respect to the real materials, where we have one or more dispersing bands.

The  $GW$  self-energy of a real system can still be written in the form of electron-boson coupling, but more poles appear [38]. For each state  $\ell$ , its diagonal matrix element contains the sum of all valence and conduction states  $j$  coupled with many different bosonic excitations  $s$ , and the time-ordered self-

energy reads

$$\Sigma_{xc}^{\ell\ell}(\omega) = \sum_{j,s \neq 0} \frac{|V_{\ell j}^s|^2}{\omega - \varepsilon_j + (\omega_s - i\eta)\text{sgn}(\mu - \varepsilon_j)}. \quad (13)$$

Here  $\varepsilon_j$  are the quasiparticle energies,  $\omega_s = E(N, s) - E(N, 0)$  are the neutral excitation energies that correspond to the energy differences between the  $N$ -particle excited state  $s$  and the  $N$ -particle ground state, and  $V_{\ell j}^s$  are the fluctuation potentials, which determine the strength of the electron-boson coupling. Often, the sum over excitations  $s$  can be approximated by a small number of dominant excitations, such as plasmons. In the following, we will disentangle the different contributions by examining separately the various ingredients entering Eq. (13), and hence the cumulant expansions for  $G$  in Eqs. (8) and (9).

In a solid, it is convenient to analyze the loss function  $L(\mathbf{q}, \omega)$ , which can be directly measured by inelastic x-ray scattering (IXS) or electron-energy-loss spectroscopies (EELS) [47]:

$$L(\mathbf{q}, \omega) = -\text{Im } \epsilon_M^{-1}(\mathbf{q}, \omega) = \frac{\epsilon_2(\mathbf{q}, \omega)}{\epsilon_1^2(\mathbf{q}, \omega) + \epsilon_2^2(\mathbf{q}, \omega)}, \quad (14)$$

where  $\epsilon_M = \epsilon_1 + i\epsilon_2$  is the complex macroscopic dielectric function. The peaks of the loss function, which generally depend on the wave vector  $\mathbf{q}$  (i.e., the experimental momentum transfer), correspond to the neutral excitations  $\omega_s$  in (13). In particular, the plasmon energies  $\omega_{pl}(\mathbf{q})$  correspond to the peaks in the loss function for which  $\epsilon_1(\mathbf{q}, \omega_{pl}(\mathbf{q})) = 0$ .

Equation (13) shows that the self-energy is an average over the couplings of the single-particle states  $\ell$  with the plasmons (and other electron-hole excitations) at all momentum transfers  $\mathbf{q}$ . As a consequence, the plasmon energy  $\omega_{pl}(\mathbf{q} = 0)$  is in general different from the plasmon satellite energies  $\omega_{ps}$  in the spectral function, which for each state are defined as the energy distance between the quasiparticle and first plasmon satellite.

In the GWA the inverse dielectric function  $\epsilon^{-1}$  and the loss function are often calculated within the random-phase approximation (RPA). However, one may go beyond the RPA by using time-dependent density-functional theory (TDDFT) [48,49], where the solution of the Dyson equation for the polarizability  $\chi = \chi_0 + \chi_0(v_c + f_{xc})\chi$  yields  $\epsilon^{-1} = 1 + v_c\chi$ . While the RPA corresponds to setting the exchange-correlation kernel  $f_{xc}$  to 0 and evaluating the independent-particle polarizability  $\chi_0$  in some mean-field approximation, the most widely used approximation in TDDFT is the adiabatic local-density approximation (ALDA) [50,51]. In general, the ALDA yields plasmon spectra in better agreement with EELS and IXS experiments than the RPA [52,53]. Therefore we will investigate whether the ALDA also improves plasmon satellites in photoemission spectra.

### III. TIME-ORDERED VERSUS RETARDED CUMULANT APPROXIMATION

The RC has been applied to the homogeneous electron gas [35], but it remains interesting to investigate whether the RC improves over the TOC for the spectral function of a real metal like sodium. To this end, we perform *ab initio* TOC and RC calculations for bulk sodium, using the computational ingredients summarized in the Appendix. The TOC and RC



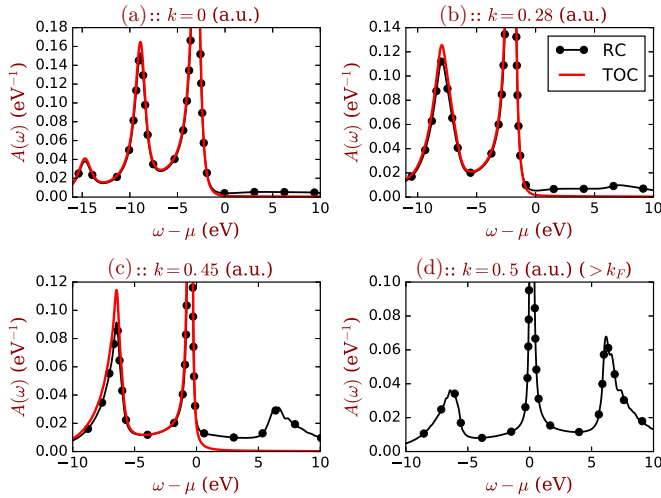


FIG. 1.  $\mathbf{k}$ -resolved spectral functions  $A(\mathbf{k}, \omega)$  for the sodium valence band along  $\Gamma N$  using TOC (red solid curve) and RC (black dotted curve). The Fermi wave vector is  $k_F = 0.49$  a.u.

results are compared in Fig. 1, which shows the  $\mathbf{k}$ -resolved spectral functions  $A(\mathbf{k}, \omega)$  along the  $\Gamma N$  direction for the sodium valence band, crossing the Fermi level at  $k_F \sim 0.49$  a.u. At  $\mathbf{k} = \Gamma$ , which is at the bottom of the band, and for states close to it, the TOC and the RC spectral functions are very similar for  $\omega < \mu$ . In agreement with previous TOC calculations [8, 16], there is a prominent quasiparticle peak which has a parabolic dispersion (see Fig. 2) and two satellites that follow the quasiparticle dispersion at a distance of  $\sim 5.84$  eV and  $\sim 11.64$  eV to the quasiparticle band, respectively. This similar dispersion is analogous to the situation in silicon, which has been investigated in [15, 17]. The satellites are slightly more intense in the TOC than in the RC, as the renormalization factors are different in the two cases. For  $\omega > \mu$ , the RC displays a nonzero spectral weight, while the TOC is always 0 by definition. This tail in the RC comes from the integration of

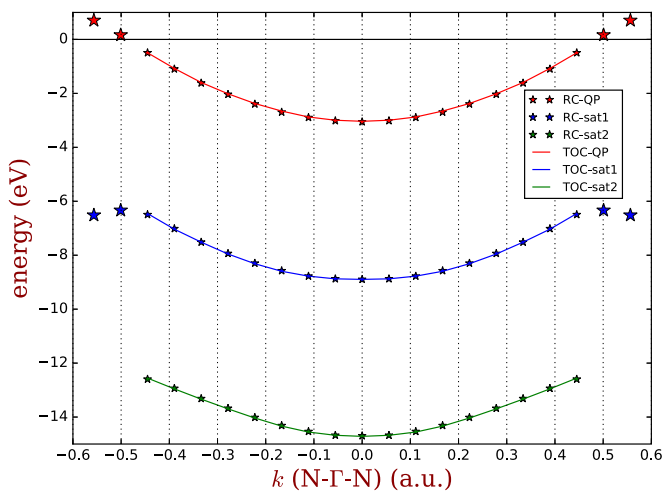


FIG. 2. The dispersion of quasiparticles (red) and first (blue) and second (green) satellites in TOC (solid curves) and RC (stars). The stars with double size are satellites from states above the Fermi level  $\mu$ .

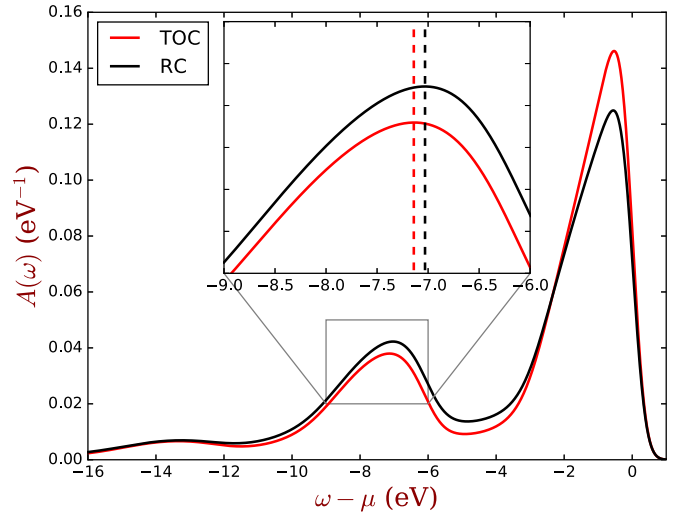


FIG. 3. The total  $\mathbf{k}$ -summed spectra for the sodium valence band in both TOC (in red) and RC (in black), multiplied by the room temperature Fermi function. Inset: Zoom on the first satellite. The two dashed vertical lines mark the positions of the maximum of each satellite; their distance is 0.11 eV.

the electron part of  $\text{Im} \Sigma_{xc}$ , which is present in the RC but not in the TOC. By approaching  $k_F$  the differences between TOC and RC spectral functions become significant: the unoccupied part of the RC spectral function becomes larger, also showing a pronounced satellite at about 6 eV above  $\mu$ . For  $k \sim k_F$  the RC is symmetric around  $\mu$ . Finally for  $k > k_F$  [see Fig. 1(d)] we show only the RC, since this matrix element of the hole TOC is zero. Interestingly, for  $k > k_F$  the RC still has a satellite for  $\omega < \mu$ , which might be measurable by photoemission experiments.

Figure 2 shows the dispersion of the band and the satellites. While for occupied states the QP and the satellites have the same parabolic dispersion, for unoccupied states we find that the satellites in the RC spectral function below the Fermi level, which are denoted by stars in the figure, do not follow the parabolic dispersion of the quasiparticle band, becoming more flat and even inverting the curvature. This behavior can be understood using the model equations (7), (9), and (10), by varying the energy  $\varepsilon_2$  in order to simulate the dispersion of the empty state.

Figure 3 shows the valence spectral functions summed over the first two bands, integrated over all  $\mathbf{k}$  in the Brillouin zone, and multiplied by the Fermi function for  $T = 300$  K together with a 0.3 eV Gaussian broadening. While qualitatively similar, the TOC and RC display small quantitative differences for both the QP peak at the Fermi level and the satellites (see the zoom around the first satellite in the inset of Fig. 3). Notably the maximum of the first satellite is more intense and closer to the QP peak in the RC compared to the TOC. The differences between TOC and RC are due to the different renormalization factors and to the satellites of the unoccupied states for  $\omega < \mu$ , which are present only in the RC spectral functions.

The maximum of the RC satellite has a binding energy that is 0.11 eV smaller than that of the TOC, bringing it into better agreement with experiment. We conclude that the RC leads to some small but visible changes in the valence photoemission

spectra of a metal such as sodium. Since the RC contains additional physics, one may expect that this approximation is better than the TOC. In the following we will present only RC spectral functions.

#### IV. ENVIRONMENT EFFECTS ON THE PLASMON SATELLITES

In this section we will study various contributions that have a small but visible influence on the satellites, while they do not affect the quasiparticles. It should be noted that all effects discussed here lead to changes of the same sign, such that they add up and finally have a non-negligible impact on the spectra.

##### A. The lattice potential: Comparing sodium and the homogeneous electron gas

Sodium is the closest realization of the homogeneous electron gas (HEG) model: the potential due to the ionic lattice introduces only a very small perturbation of the ideal HEG, the valence-band dispersion remains close to parabolic, and the Fermi surface close to spherical. The spectral function of the HEG has been previously calculated using both the TOC [54–56] and the RC [35,36] that we employ here. By comparing sodium and the HEG with the same electron density, here we can additionally establish whether the lattice potential influences the quasiparticle and satellite properties in the same way.

The integrated spectral functions for Na and the HEG, which are displayed in Fig. 4, are very similar for the quasiparticle peak at the chemical potential  $\mu$ , whereas their satellites are slightly different (see the zoom in the inset of Fig. 4). In the HEG the satellite has a larger distance from the quasiparticle than in Na, resulting in a larger binding energy. This is confirmed by comparing in Fig. 5 the dispersion of the  $\mathbf{k}$ -resolved spectra along  $\Gamma\text{N}$ . While the quasiparticle bands overlap entirely in the two cases, at each  $\mathbf{k}$  point the distance

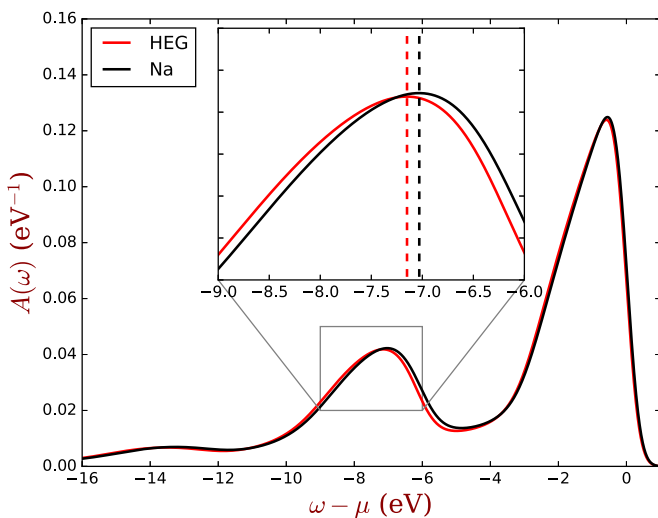


FIG. 4. The total  $\mathbf{k}$ -summed spectra of HEG (in red) and sodium (in black), multiplied by the Fermi function. Inset: Zoom on the first satellite. The two dashed vertical lines mark the positions of the maximum of each satellite; their distance is 0.12 eV.

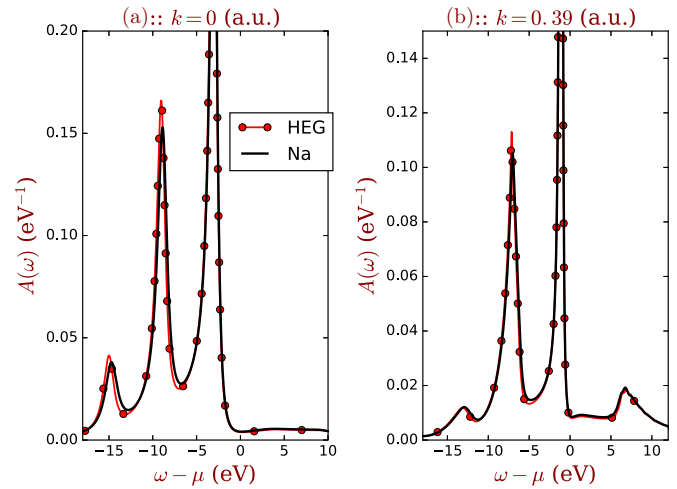


FIG. 5.  $\mathbf{k}$ -resolved spectral functions  $A(\mathbf{k}, \omega)$  of sodium (red curve with circles) and the HEG (black curve) at the  $\Gamma$  point and close to Fermi level ( $k_F \sim 0.49$  a.u.).

between the quasiparticle and the first satellite is larger in the HEG than in Na. This difference is almost twice as big for the second satellite [see Fig. 6(a)]. We also note that the largest differences occur around the  $\Gamma$  point at the bottom at the band, while around the Fermi level the satellite positions get closer.

For a better comparison, Figs. 6(b) and 6(c) show for both sodium and the HEG the dispersion of the quasiparticle band and the plasmon satellites, where the satellite energies have been shifted such that they coincide with the quasiparticle at  $\Gamma$ . As already found in sodium (see Fig. 2), also in the HEG at the bottom of the band the satellite band follows the parabolic dispersion of the quasiparticle. When the state is instead close to Fermi level, there is an abrupt change, yielding a flat dispersion and a downwards bending. Since this feature

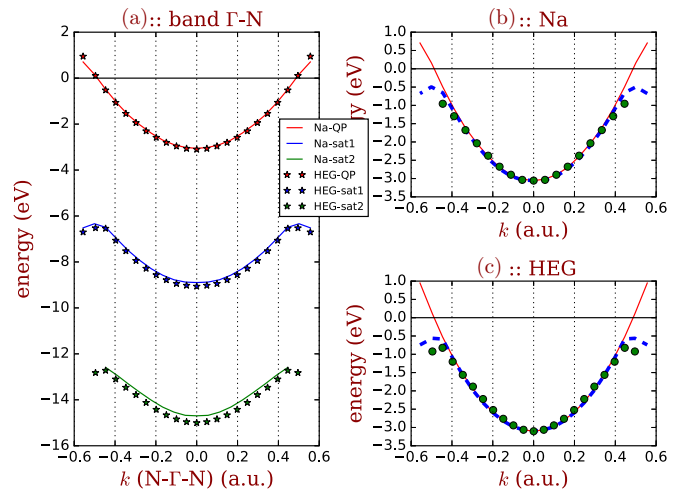


FIG. 6. (a) Dispersion of quasiparticles (in red) and first (in blue) and second (in green) satellite of sodium (solid curves) and of the HEG (stars) along the  $\text{N}\Gamma\text{N}$  direction. (b), (c) Comparison of the quasiparticle (red solid curves), first satellite (blue dashed curve), and second satellite (green dots) dispersions of (b) sodium and (c) the HEG. The satellite energies have been shifted in order to align all energies at the  $\Gamma$  point.

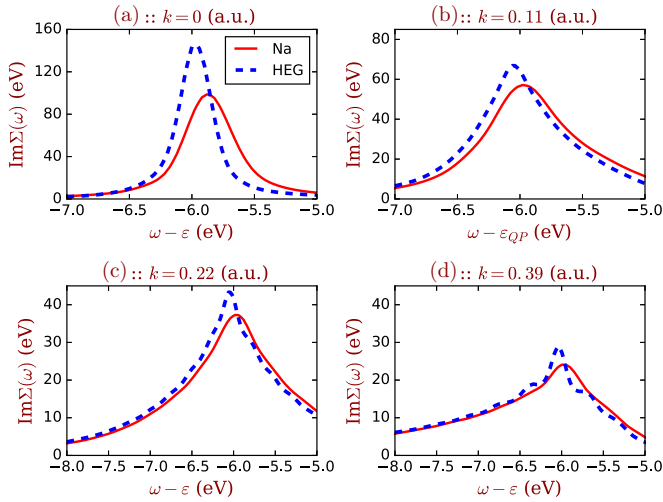


FIG. 7. The shifted imaginary part of self-energy of sodium (red solid lines) and HEG (blue dashed lines) at different  $\mathbf{k}$  points along  $\Gamma\text{N}$  in the sodium Brillouin zone. Only the removal part  $\omega < \mu$  is shown. The Fermi wave vector is at  $k_F = 0.49$  a.u.

is in common to the HEG and Na, this property of the satellite dispersion must be due to the electronic interaction, while the differences in the satellite energies between the HEG and Na are caused by the lattice potential.

In order to understand the origin of these differences, let us analyze the imaginary part of the self-energy  $\text{Im} \Sigma_{xc}$  that enters Eq. (9), shown in Fig. 7. In both sodium and the HEG,  $\text{Im} \Sigma_{xc}$  is characterized by a single peak, which in the HEG is located at larger distances from the corresponding quasiparticle peak than in Na (note that the energy scale in the figure is given relative to the quasiparticle energy). This explains why the satellites in the spectral functions are at higher binding energies in the HEG.

Approaching the Fermi level, the difference between sodium and the HEG decreases, while the peak becomes broader and asymmetric. The shape of  $\text{Im} \Sigma_{xc}$  can be directly linked, through Eq. (13), to the parabolic valence band dispersion in Na and in the HEG. Typically, for a given bosonic excitation  $s$ , the dominant contribution to the sum over states  $j$  is selected by the coupling matrix elements  $V_{\ell j}^s$  and stems from states that are close; i.e.,  $\text{Im} \Sigma_{xc}^{\ell\ell}$  is dominated by contributions with  $|\mathbf{k}_j - \mathbf{k}_\ell| < \Delta$ . When  $\mathbf{k}_\ell$  is at the bottom of the parabolic band, i.e., close to  $\Gamma$  where the band is relative flat, neighboring states  $\mathbf{k}_j$  for which  $V_{\ell j}^s$  is significantly different from zero have energies  $\varepsilon_j$  very close each other. As a result,  $\text{Im} \Sigma_{xc}^{\ell\ell}$  for such a state  $\ell$  has a sharp peak around  $\varepsilon_\ell - \omega_s$ . Instead, when  $\mathbf{k}_\ell$  is away from  $\Gamma$ , where the band has a steeper slope,  $\text{Im} \Sigma_{xc}^{\ell\ell}$  is different from zero in a wider energy range. At the same time, it becomes more asymmetric, developing a long tail on the low-energy side. The reason for the asymmetry is the availability of energies: close to the Fermi level, there are fewer occupied states  $j$  with energy  $\varepsilon_j > \varepsilon_\ell$ , whereas many states with smaller energies  $\varepsilon_j < \varepsilon_\ell$  contribute to the low-energy tail of the peak. Going towards the bottom of the valence band, the spectral weight continuously moves towards the high-energy side of the peak. At the bottom of the band, however, the asymmetry is hidden by the fact that the peak is sharp. Of course, this is a qualitative analysis, since the coupling with

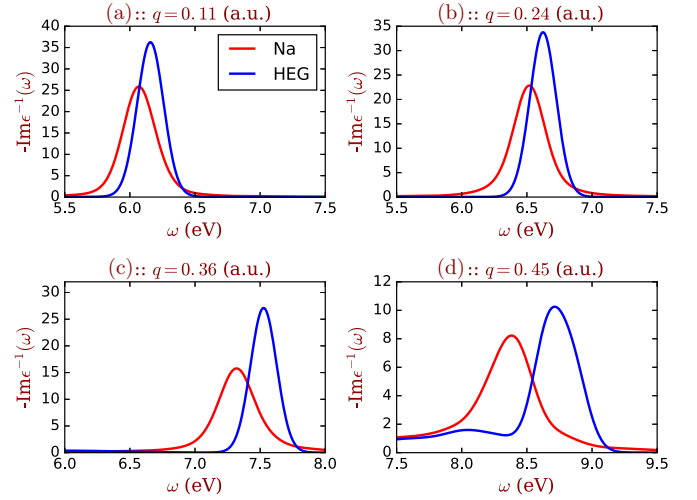


FIG. 8. The RPA loss functions of sodium (red curve) and HEG (blue curve) at different momentum transfers  $q$  (in a.u.).

bosonic excitations of different character and energies  $\omega_s$  that are summed up to form the self-energy complicates the picture.

Finally, in order to understand why the peak position of  $\text{Im} \Sigma_{xc}$  in the HEG is always farther from the quasiparticle than in Na, we compare the loss functions, which are shown in Fig. 8 as a function of momentum transfer  $q$ . For  $q$  smaller than the wave vector  $q_c \sim 0.45$  a.u., the peak in the loss function corresponds to a plasmon resonance, for which  $\varepsilon_1 = 0$  [see Eq. (14)]. Above  $q_c$  the plasmon enters the electron-hole continuum where the loss function is dominated by  $\varepsilon_2$ . In agreement with Ref. [57], the HEG shows larger plasmon energies than sodium at all momentum transfers. As  $q$  increases, the difference becomes larger and larger: the plasmon in sodium is more and more affected by band-structure effects and short-range spatial inhomogeneities in the charge response become more apparent. These observations suggest that low-density regions have a stronger influence on the plasmon energy of an inhomogeneous material than high-density regions, such that the resulting plasmon energy is smaller than what one would expect from the average density.

This difference in the plasmon energies explains why the plasmon satellite has a larger binding energy in the HEG than in Na. Since the difference in the peak position of  $\text{Im} \Sigma_{xc}$  between sodium and the HEG is always smaller than 0.2 eV (see Fig. 7), we can conclude that the loss functions at small momentum transfers (i.e.,  $q \lesssim 0.3$  a.u., where the loss functions of the HEG and Na are similar) are those which contribute mostly to  $\text{Im} \Sigma_{xc}$  and hence to the position of the plasmon satellite in the spectral functions.

## B. Thermal expansion

The results above have been obtained with calculations performed at temperature  $T = 0$ , and with a lattice parameter for sodium of 4.227 Å, which is the experimental result measured at  $T = 5$  K. However, experiments are often performed at room temperature,  $T = 293$  K. There is no major influence of the electronic temperature, besides the Fermi function in the spectra on this range of temperatures, but thermal expansion may play an important role. Indeed, by increasing the temperature

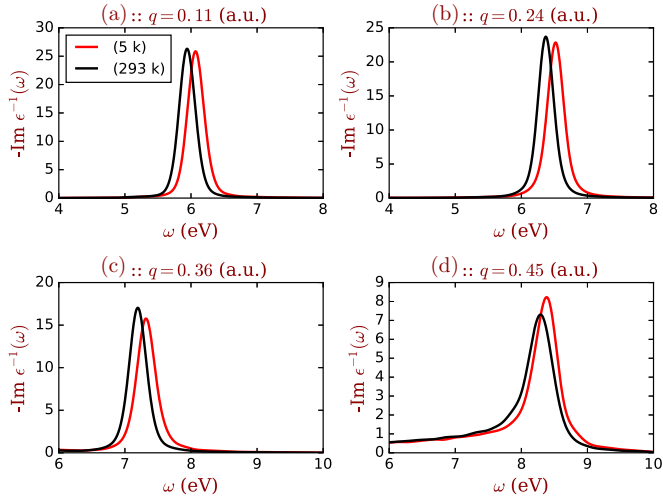


FIG. 9. RPA loss functions of sodium calculated with lattice parameters corresponding to 5 K (red curve) and 293 K (black curve) at different momentum transfers  $q$  (in a.u.).

from 5 K to room temperature, the lattice parameter of sodium changes considerably, from 4.227 Å to 4.29 Å [58]. Since the plasmon energy at  $\mathbf{q} = 0$  is approximately proportional to the square root of the electronic density, we expect that with the decrease of density at higher temperature, the plasmon energy decreases as a consequence of the lattice thermal expansion. Indeed, in Fig. 9 we find that for all momentum transfers the plasmon resonance is located at lower energies in the loss function calculated with the room temperature lattice parameter than in the 5 K result.

Extrapolating from the comparison between Na and the HEG in Sec. IV A, one should expect a similar effect on the spectral functions. Indeed, for all  $\mathbf{k}$  points, the plasmon satellites in Figs. 10 and 11 have smaller binding energies at room temperature than at 5 K. Again, the satellites are more affected by the thermal expansion than the QP peaks, which remain almost unchanged.

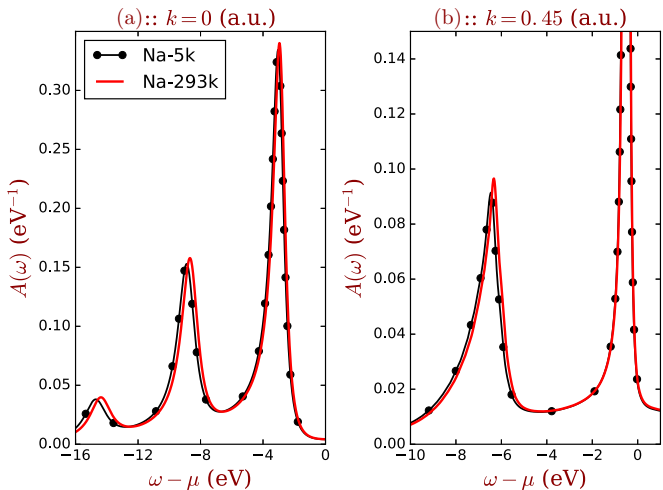


FIG. 10.  $\mathbf{k}$ -resolved spectral functions of sodium along the  $\Gamma N$  direction using lattice parameters corresponding to 5 K (black curve with dots) and 293 K (red solid curve) at the  $\Gamma$  point and close to Fermi level ( $k_F = 0.49$  a.u.).

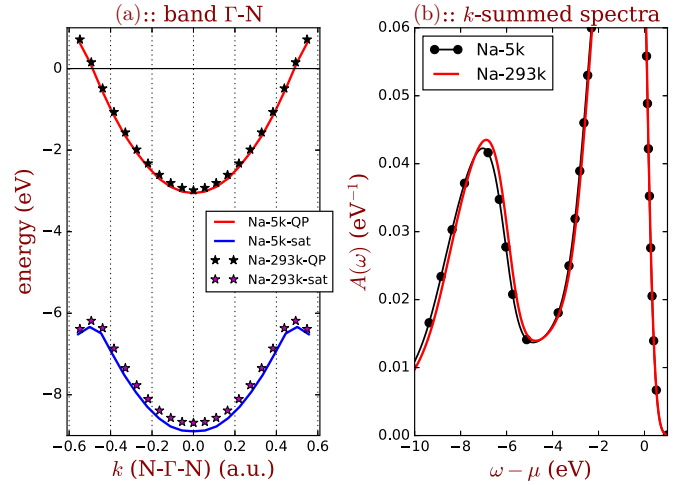


FIG. 11. (a) The QP and plasmon satellite dispersions along  $\Gamma N$ . The QP and first satellite energies of Na at 5 K are represented in red and blue solid curves, respectively. For Na at 293 K QP and satellite energies are stars. (d) The total spectra summed over  $\mathbf{k}$  points and two bands, using lattice parameters corresponding to 5 K (black curve with dots) and 293 K (red solid curve).

This trend is confirmed by a calculation where we have artificially expanded the lattice parameter to 4.44 Å for the sake of demonstration. Figure 12 shows that the satellite band moves much closer to the QP band, which does change, but to a much lesser extent: while the QP bandwidth is reduced by 0.28 eV, the binding energy of the maximum of the satellite peak decreases by 0.46 eV.

### C. Core polarization

Transition from shallow core levels to empty states are known to affect the loss function also at lower energies, i.e., in the energy range of valence transitions [59–61]. Since we have

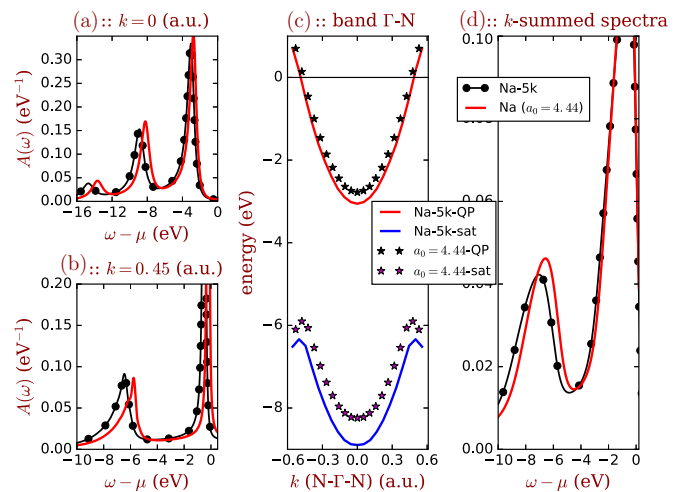


FIG. 12. Comparison between Na with lattice parameter at 5 K ( $a_0 = 4.23$  Å) and Na with artificially expanded lattice parameter ( $a_0 = 4.44$  Å):  $\mathbf{k}$ -resolved spectral functions (a) at the  $\Gamma$  point and (b) close to the Fermi level; (c) band and satellite dispersions; (d)  $\mathbf{k}$ -integrated spectral function.



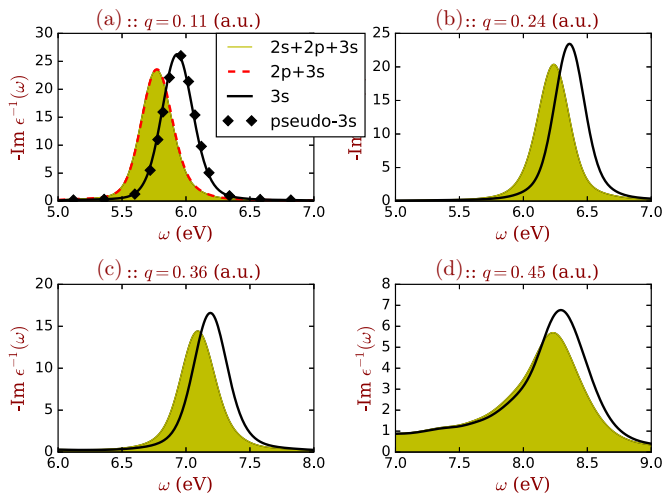


FIG. 13. The loss functions  $-\text{Im} \epsilon^{-1}$  including different transitions. The yellow filled curve contains all transitions from  $2s$ ,  $2p$ ,  $3s$  states. The red dashed and black solid curves contain transitions from  $2p + 3s$  and  $3s$  only, respectively. The black diamonds are calculated using a pseudopotential containing only  $3s$  electrons as valence states.

found that the satellite in the spectral function is very sensitive to small changes of the plasmon properties, here we analyze whether those core polarization effects have an influence also on the valence plasmon satellites in the spectral function of sodium.

In order to investigate how the  $2s$  and  $2p$  core states affect the loss function we have used two different pseudopotentials: one that has only  $3s$  as valence electrons and another where also  $2s$  and  $2p$  are explicitly included in the calculations [62]. First of all, we have to make sure that the errors inherent in the pseudopotential approach do not bias our conclusions. To this end, we have verified that the two pseudopotentials give the same result when only excitations from  $3s$  states are taken into account. This is indeed the case, as one can see from the comparison of the two pseudopotential results (black diamonds and black curve) in Fig. 13(a). In the next step, we add transitions from  $2s$  and  $2p$  core levels to the calculations. This leads to the yellow shaded curves, which are redshifted with respect to the black curves for all momentum transfers [see Figs. 13(a)–13(d)]. This effect is mainly due to the  $2p$  electrons: results with (yellow shaded curves) or without [red curve in Fig. 13(a)] the  $2s$  are indistinguishable.

To understand the origin of the redshift of the loss function, the real and imaginary parts of the dielectric functions at momentum transfers  $q = 0.11$  a.u. and  $q = 0.45$  a.u. are shown in Figs. 14 and 15, respectively. When the transitions from core levels are included in the calculation, at smaller energies  $\epsilon_2$  is unchanged, but at energies larger than 25 eV, which corresponds to the core-level binding energies, a new structure appears. As a consequence, through the Kramers-Kronig relation,  $\epsilon_1$  is affected on a wider energy range. In particular the position of its crossing with the zero axis is shifted, which changes the plasmon peak in the loss function. This effect is smaller at larger momentum transfers.

The core-polarization effect in the loss functions influences the spectral functions for the sodium valence band (see

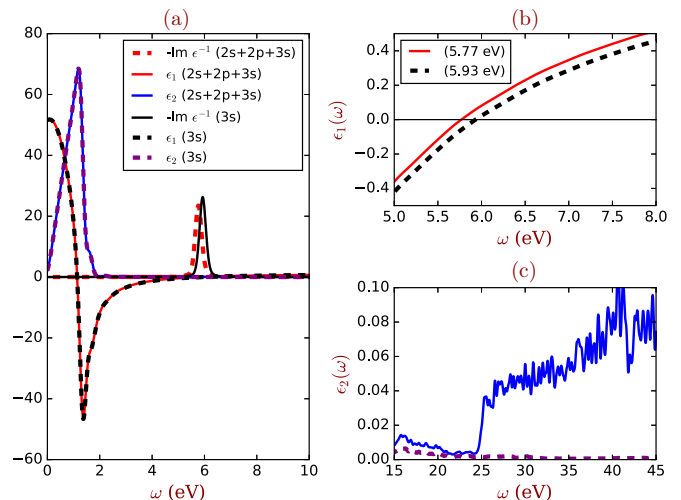


FIG. 14. (a) The loss functions  $-\text{Im} \epsilon^{-1}$  containing the core transitions (red dashed curve) and transitions of valence states only (black solid curve), together with their real ( $\epsilon_1$ ) and imaginary ( $\epsilon_2$ ) parts at  $q = 0.11$  a.u. (b) Zoom around the plasmon energy for  $\epsilon_1$ . (c) Zoom around the core-level contributions for  $\epsilon_2$ . Note that the fast wiggles in the blue curve in panel (c) are due to the finite  $\mathbf{k}$ -point sampling.

Fig. 16). As in the previous cases, the QP peak is affected in a negligible way, while the plasmon satellite energy in the  $\mathbf{k}$ -integrated spectral function (see Fig. 17) is reduced by about 0.23 eV by including the core-level transitions in the screening calculation.

Altogether, the results presented in this and the previous two sections clearly illustrate that the plasmon satellite is very sensitive to all the changes of the environment surrounding the quasiparticle excitation. The lattice potential, the change in the lattice parameter, and the polarization from the core electrons have a much stronger influence on the plasmon satellites than on the quasiparticle peaks. This finding is consistent with other observations; in particular, the drastic modification of plasmon excitations in bulk and at surfaces of Cu and Ag due to polarization of occupied  $d$  bands [63]. Another example is the

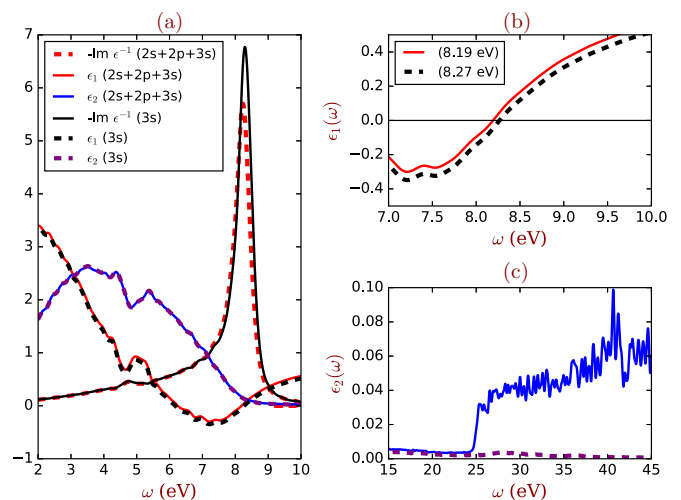


FIG. 15. Same as Fig. 14, but for  $q = 0.45$  a.u.

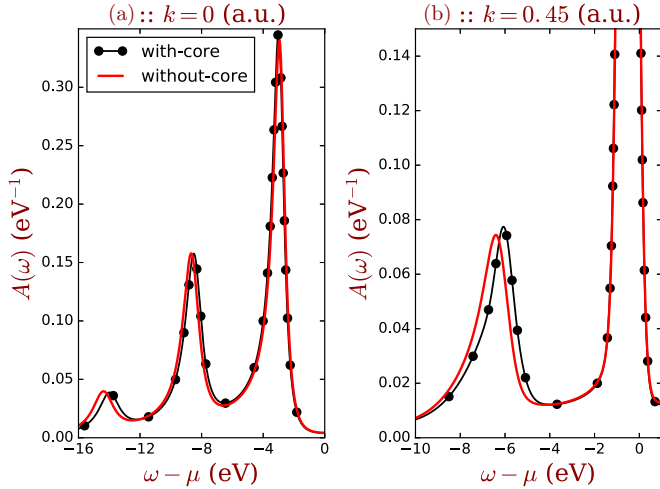


FIG. 16.  $\mathbf{k}$ -resolved spectral functions  $A(\mathbf{k}, \omega)$  of sodium taking into account the core polarization (black curve with dots) and without core polarization (red curve) (a) at the  $\Gamma$  point and (b) close to Fermi level ( $k_F = 0.49$  a.u.).

comparison of graphene and graphite in Ref. [12]: also in that case it was found that the presence of neighboring graphene planes in graphite affects more the satellite than the QP spectra. This implies that plasmon satellites in photoemission spectra are powerful “detectors” for small variations of a material, and that measuring and analyzing the satellites in photoemission spectra, in addition to the quasiparticle peaks, may give additional precious information.

**V. THE SCREENED INTERACTION BEYOND THE RPA**

In the GWA the screening given by the inverse dielectric function  $\epsilon^{-1}$  is usually calculated at the level of the RPA. However, previous studies have shown that in sodium, like in other materials, the ALDA yields loss functions in better agreement with IXS experiments [57,61], since it leads to a redshift of the plasmon energy that increases with the

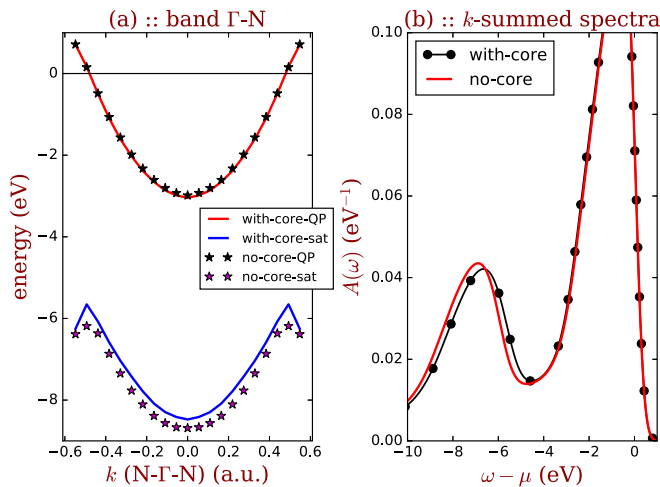


FIG. 17. (a) Band and satellite dispersions along  $\Gamma N$  and (b)  $\mathbf{k}$ -integrated spectral function, calculated with or without the core polarization contribution.

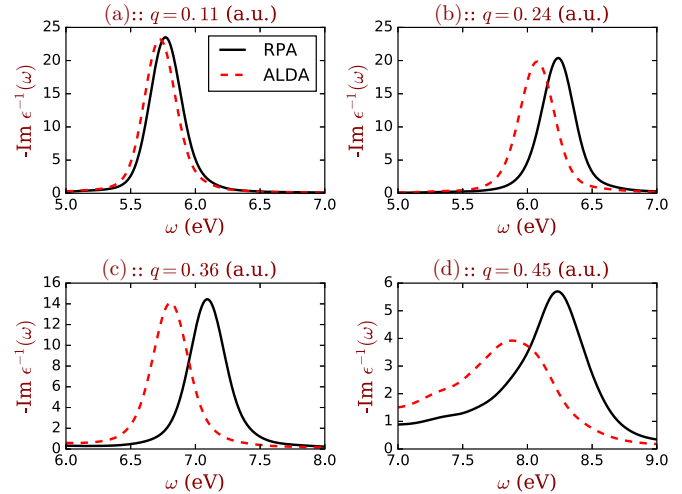


FIG. 18. The loss functions  $-\text{Im } \epsilon^{-1}$  of Na calculated in RPA (black solid lines) and ALDA (red dashed lines) at different momentum transfers  $\mathbf{q}$  in a.u.

momentum transfer. This is confirmed by the results reported in Fig. 18. One would therefore expect that the choice of the ALDA or the RPA for the calculation of the screening should significantly affect the plasmon satellites. On the other hand, our previous analysis shows that the satellite position in the spectral function is mainly determined by the plasmon energy at small momentum transfers, where the difference between the RPA and the ALDA and the difference between the RPA and experiment are minor. This raises the question of how important it is to go beyond the RPA in the calculation of plasmon satellites, and whether the calculation that yields loss functions in better agreement with IXS measurements also yields plasmon satellite spectra in better agreement with photoemission experiments. This is a nontrivial question, and we can only give evidence, since the quality of many-body perturbation theory (MBPT) results is often influenced by error canceling.

Going beyond the RPA for  $W$  corresponds to the inclusion of vertex corrections beyond the GWA for  $\Sigma_{xc}$ , which has been an issue of intense research for decades. In agreement with results from the literature [64–67], here we find that passing from RPA to ALDA the QP bandwidth decreases by 0.22 eV, while the QP peaks increase slightly their width, implying a reduction of the QP lifetimes [66] (see Fig. 19).

In line with the findings in the previous section, also in this case we find that the change in the screening affects more the satellites than the QPs [see Fig. 20(a)]: the quasiparticle binding energy at  $\Gamma$  is reduced by 0.22 eV due to the ALDA, while the satellite binding energy decreases by 0.37 eV. This leads to a decrease of the distance between the QP and the satellite of 0.15 eV, going from RPA to ALDA. Also in the  $\mathbf{k}$ -integrated spectral function [see Fig. 20(b)], both the increase of the QP width and a slight reduction of the binding energy of the center of mass of the satellite peak are apparent. This means that using the ALDA instead of the RPA for the calculation of  $W$ , spectral functions are obtained in slightly better agreement with photoemission experiments. The comparison with experiment will be discussed more in detail in the next section.

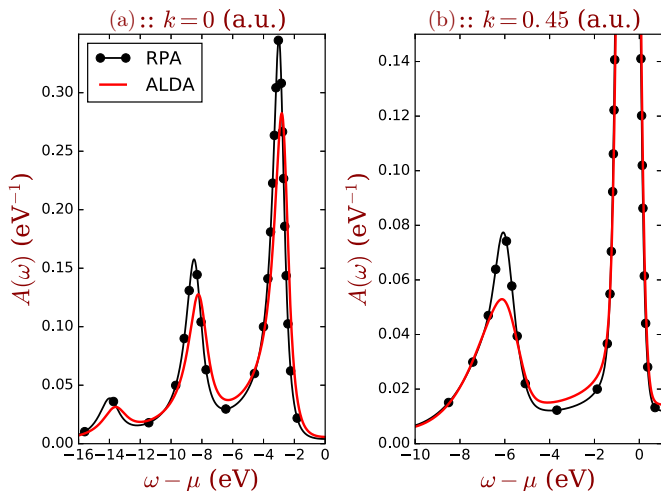


FIG. 19.  $\mathbf{k}$ -resolved spectral functions  $A(\mathbf{k}, \omega)$  of sodium using RPA (black dotted curve) and ALDA screening (red curve) (a) at the  $\Gamma$  point and (b) close to Fermi level ( $k_F = 0.49$  a.u.).

## VI. COMPARISON WITH EXPERIMENT

In Ref. [16] the spectral function of the sodium valence was calculated using the TOC together with RPA screening, the 5 K lattice constant, and a valence-only pseudopotential. Moreover, in the calculation of the self-energy the screened interaction  $W(\mathbf{q})$  is summed over wave vectors  $\mathbf{q}$ , and it is difficult to evaluate the intraband contribution for  $\mathbf{q} = 0$ . Since this contribution is vanishing when the sum is converged with respect to the number of  $\mathbf{q}$  points, the intraband contribution for  $\mathbf{q} = 0$  was neglected in Ref. [16] and in the present work. For any finite  $\mathbf{q}$ -point sampling, however, this neglect is an approximation. We have checked that it introduces an error of 0.2 eV for the  $\mathbf{q}$ -point mesh that was used in Ref. [16]. (Note that the results presented here are different since we take intraband contributions for  $\mathbf{q} = 0$  approximately into account, as explained in Appendix, and therefore obtain much better convergence.) Altogether, a discrepancy with experiment of almost 1 eV was found concerning the distance between

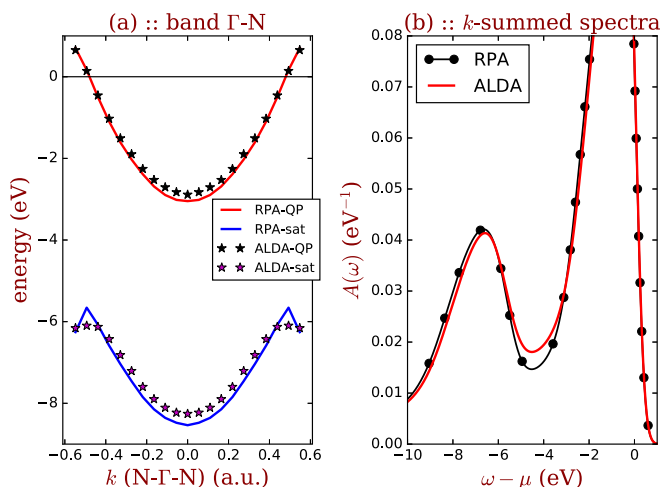


FIG. 20. (a) Band and satellite dispersions and (b)  $\mathbf{k}$ -integrated spectral functions of sodium using RPA and ALDA screening.

the first plasmon satellite and the valence band, and it was speculated that the RPA might be at least partially responsible for this difference. As we have seen in the previous sections, the RPA does indeed lead to an overestimate of the QP-satellite distance of 0.15 eV, but several other effects add up: together with the effects of the lattice constant (0.15 eV), the core polarization (0.23 eV), the intraband contribution (0.2 eV), and the use of the RC instead of the TOC (0.11 eV), the total improvement amounts to a significant change of about 0.84 eV.

While the comparison of peak positions with the experimental ones can be done on a quantitative level, the comparison of spectra including spectral weight and shapes is more delicate. For sodium, the ARPES data of Jensen *et al.* [68,69] displayed a bandwidth reduction due to interaction effects that was larger than predicted from HEG calculations, and a sharp peak at the Fermi energy for photon energies where no hole excitation should be possible in a single-particle picture. These experimental results gave rise to controversial interpretations [70,71], with Overhauser [72] proposing that the observed sharp peak close to the Fermi level was a signature of the existence of a charge-density wave, while Mahan and coworkers [73–75] showed that a careful description of the photoemission process itself was needed to reconcile theory and experiment. This debate illustrates that for a detailed comparison with experimental photoemission spectra, the calculation of the intrinsic spectral function alone is not sufficient. However, the simulation of the photoemission process is a complex task itself. We therefore limit ourselves to a semiquantitative comparison of spectra, following the simplified approach used [85] in Refs. [6,16].

The photoelectron leaving the sample undergoes scattering events: these extrinsic losses sum with the additional excitations induced by the photohole that are seen as satellites in the intrinsic spectral function. Moreover, the interaction of the photoelectron and the photohole produces an interference effect that partially cancels with intrinsic and extrinsic contributions. In order to take into account these extrinsic and interference effects in the calculation of the photocurrent, we adopt the model of Hedin and coworkers [76,77]. Since this approach has been developed for the time-ordered formalism only, here we discuss these effects on the basis of the TOC spectral function. We also included the secondary electron background using a Shirley profile [78]; we multiplied the calculated spectral functions with a Fermi function for  $T = 300$  K and applied a Gaussian broadening of 0.255 eV corresponding to the experimental resolution [37]. The final comparison between the calculated photocurrent for photon energy  $h\nu = 1487$  eV and the experimental data from Ref. [37] is shown in Fig. 21.

The TOC intrinsic (black dashed curve) and intrinsic plus extrinsic and interference effects (solid curve) spectral functions are almost identical [86] to the results of Ref. [16], with its overestimate of the QP-satellite distance of 0.8 eV, since besides a lightly different broadening (0.3 eV in [16], 0.25 eV in the present work) the curves have been calculated using the same ingredients: RPA screening without intraband contributions, a valence-only pseudopotential, and the 5 K lattice constant. Our best intrinsic spectral function, namely the RC result obtained at the room temperature lattice constant and with ALDA screening including core polarization as well

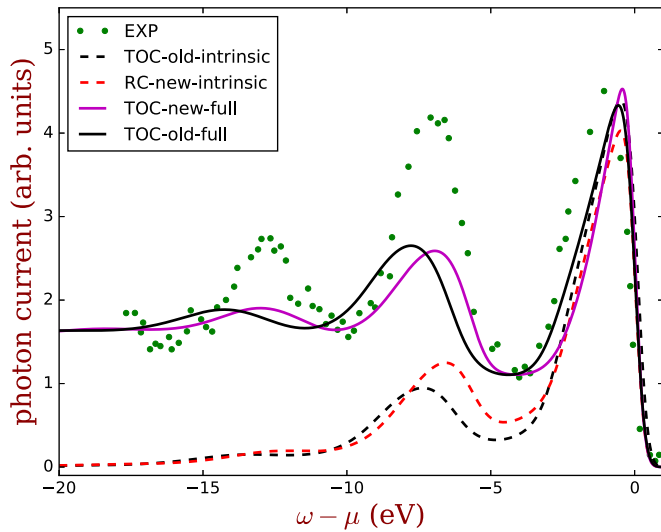


FIG. 21. The black and red dashed curves are intrinsic TOC from Ref. [16] (using the 5 K lattice constant, transitions from valence only, without intraband transitions, and RPA screening) and RC spectral functions (using room temperature lattice constant, including transitions from semicore and intraband transitions, and ALDA screening), respectively. The TOC spectral function (using the 5 K lattice constant, transitions from valence only, without intraband transitions, and RPA screening) with extrinsic and interference effects, together with secondary electron background (magenta solid curve), is compared with experimental data from Ref. [37] (green dots). The black solid curve is obtained by adding the extrinsic and interference effect on the black dashed curve. All curves have been aligned on the low-binding energy side of the QP.

as intraband contributions, is given by the red dashed curve. The quasiparticle peak of the two results is similar (the QP maximum of the red and black dashed curves is at 0.49 and 0.68 eV binding energy, respectively). However, it can be clearly seen that as outlined above, the binding energy of the first plasmon satellite in the new calculation is about 0.8 eV smaller than the old one, thus reducing significantly the difference with respect to experiment. This can be better appreciated when the full photoemission experiment is simulated as explained above (magenta curve). Concerning the spectral shape and intensities, more work is needed: the experimental quasiparticle is broader and slightly more symmetric than the calculated one, which may be due to several reasons, such as the experimental resolution or temperature effects beyond the change in lattice constant (e.g., phonons). Moreover also the photoionization cross sections and the presence of the surface (with the corresponding surface plasmons) are known to play a role [37]. This also leads to an uncertainty in the relative normalization of the spectra, which are given in arbitrary units, and partially explains the apparent difference in the weight of the satellites. However, our method to simulate extrinsic and interference effects is admittedly quite crude, and one should not overinterpret the results.

## VII. CONCLUSION

We have presented a detailed study of the photoemission spectra of sodium and the homogeneous electron gas, with a

focus on plasmon satellites. This study is motivated by the increasing use of cumulant expansion approximations (CEAs) for the *ab initio* calculation of photoemission spectra. While model studies in this context are numerous, many details concerning quantitative calculations remain to be elucidated.

The main conclusion of the present work is the high sensitivity of satellites to many details of the calculations and, strictly related, to many details of the real material in experiments. Noticeable changes in the satellite positions occur due to thermal expansion and due to the effect of the crystal potential. Moreover, the semicore polarization modifies the satellite positions. These effects are important to explain the measured spectra [37]. On the computational side, improvements are also found by using TDDFT in the adiabatic local density approximation instead of the RPA for the calculation of screening. Moreover, the RC version of the CEA instead of the traditional TOC leads to a further small improvement of the satellite position, and creates electron removal satellites for spectral functions at  $\mathbf{k} > \mathbf{k}_F$  which might be measurable if sufficient experimental resolution in  $\mathbf{k}$  and energy is available. A fully quantitative comparison with experiment is beyond the scope of this work, since photoemission contains many effects that go beyond the intrinsic spectral function. In particular, the inclusion of extrinsic and interference effects has up to now only been done in a very approximate way, and with a prescription that is limited to the TOC. However, our study yields detailed insight about interesting features of the intrinsic spectral functions and about the care that is needed in the calculations, and it highlights the potential impact of studies of the satellite part of photoemission spectra for the understanding of materials.

## ACKNOWLEDGMENTS

The research leading to these results has received funding from the European Research Council under the European Union's Seventh Framework Programme (FP/2007-2013), ERC Grant Agreement No. 320971, and from a Marie Curie FP7 Integration Grant. Computation time was granted by GENCI (Project No. 544). J.J.R. acknowledges hospitality by the Ecole Polytechnique, with financial support by the Labex NanoSaclay and the chaire X-ESPCI-Saint Gobain "Sciences des Matériaux et Surfaces Actives." J.J.K. and J.J.R. are supported in part by US DOE BES Grant No. DE-FG02-97ER45623. We acknowledge fruitful discussions with Marco Cazzaniga.

## APPENDIX: COMPUTATIONAL DETAILS

We carry out energy-self-consistent *GW* calculations (updating *G*, but keeping *W* fixed) using a plane-wave basis and norm-conserving Troullier-Martins-type pseudopotentials [79] as implemented in the ABINIT code [80]. This scheme can be seen as an approximation to an optimized quasiparticle calculation, such as in the quasiparticle self-consistent *GW* scheme [81]. The update of energies is consistent with Hedin's suggestion of level alignment in Ref. [38]; it is important in order to obtain the correct distance between the quasiparticle and the satellite [43,44]. The Brillouin zone (BZ) of sodium and homogeneous electron gas are both sampled using a  $20 \times$



TABLE I. Parameters used in the intraband transitions.

Systems	$\omega_p$ (eV)	$\eta$ (eV)
HEG	6.39	0.2
Na-5k (valence)	5.96	0.289
Na-293k (valence)	5.857	0.274
Na-293k-core-rpa	5.449	0.248
Na-293k-core-alda	5.383	0.242

$20 \times 20$  grid mesh that yields 145 inequivalent  $\mathbf{k}$  points in the irreducible Brillouin zone (IBZ) for sodium, and 726  $\mathbf{k}$  points for homogeneous electron gas, since sodium is face-centered cubic and our homogeneous electron gas is simulated using a simple cubic structure. A smearing temperature of 0.005 Ha was used for all the calculations. This is a fictitious temperature that only serves as a computational trick to speed up the  $\mathbf{k}$ -point convergence, which explains why we can still use a standard time-ordered formalism in the  $GW$  calculation (besides the fit of the intraband contribution to the screening; see Table I and below).

The plane-wave cutoff of the LDA ground-state calculation was 6 Ha for the homogeneous electron gas, 16 Ha for sodium with valence electrons only, and 200 Ha for sodium containing core electrons. The converged parameters for the calculation of screening and self-energy are reported in Table II, where the first part contains the parameters for screening calculation and the second part is for the self-energy calculation. The Lorentzian broadening in both  $\chi_0$  and  $\Sigma_{xc}$  [e.g.,  $\eta$  in Eq. (13)] is chosen to be 0.1 eV in all  $GW$  calculations. For the loss functions (see Figs. 8, 9, 13, 14, 15, and 18) the parameter  $\eta$  is reduced to 0.001 eV in the calculation of  $\chi_0$  and the final spectra are convoluted with a Gaussian of 0.1 eV width. Also all the spectral functions have been convoluted with a Gaussian of

TABLE II. Parameters in the  $GW$  calculations. The upper part refers to the calculation of  $W$  and the bottom part to the calculation of  $\Sigma_{xc}$ .

Parameters	HEG	Na (valence)	Na (core)
nband	30	60	60
npwwfn	50	100	1500
npweps	50	50	50
nfreqim	25	10	10
nfreqre	225	150	150
freqremax	25 eV	25 eV	25 eV
nband	30	60	60
npwwfn	50	200	9000
npwsigx	50	200	9000

0.3 eV width, except in Fig. 21, where we adopted a broadening of 0.255 eV corresponding to the experimental resolution.

In Table II, nband refers to the number of bands, npwwfn and npweps are the number of plane waves representing the wave functions and the dielectric matrix, respectively, and nfreqim and nfreqre are the number of imaginary and real frequencies, respectively. The maximum real frequency is represented by freqremax. The number of plane waves for the exchange part of the self-energy is named npwsigx.

The intraband transitions in the dielectric function for  $\mathbf{q} = 0$  are taken into account approximately using  $\epsilon_{intra} = 1 - \omega_p^2 / [\omega(\omega + i\eta)]$  [66,82] where the parameters  $\omega_p$  and  $\eta$  are fitted on the calculated retarded loss function for small  $\mathbf{q} \neq 0$  (see Table I).

The spectra of the cumulant expansion approximations are calculated using our cumulant code [83]. The cumulant code takes the outputs of the  $GW$  calculation from the ABINIT code. In particular, we evaluate Eqs. (6) and (8) for the calculation of the time-ordered cumulant, and Eq. (9) in the retarded cumulant calculation.

- [1] A. Damascelli, Z. Hussain, and Z.-X. Shen, *Rev. Mod. Phys.* **75**, 473 (2003).
- [2] L. Hedin, *Phys. Rev.* **139**, A796 (1965).
- [3] R. Martin, L. Reining, and D. Ceperley, *Interacting Electrons: Theory and Computational Approaches* (Cambridge University Press, Cambridge, United Kingdom, 2016).
- [4] B. Lundqvist, *Phys. Kondens. Mater.* **6**, 193 (1967).
- [5] C. Blomberg and B. Bergersen, *Can. J. Phys.* **50**, 2286 (1972).
- [6] M. Guzzo, G. Lani, F. Sottile, P. Romaniello, M. Gatti, J. J. Kas, J. J. Rehr, M. G. Silly, F. Sirotti, and L. Reining, *Phys. Rev. Lett.* **107**, 166401 (2011).
- [7] J. Lischner, D. Vigil-Fowler, and S. G. Louie, *Phys. Rev. Lett.* **110**, 146801 (2013).
- [8] F. Aryasetiawan, L. Hedin, and K. Karlsson, *Phys. Rev. Lett.* **77**, 2268 (1996).
- [9] F. Aryasetiawan and O. Gunnarsson, *Rep. Prog. Phys.* **61**, 237 (1998).
- [10] M. Vos, A. S. Kheifets, E. Weigold, S. A. Canney, B. Holm, F. Aryasetiawan, and K. Karlsson, *J. Phys.: Condens. Matter* **11**, 3645 (1999).
- [11] A. S. Kheifets, V. A. Sashin, M. Vos, E. Weigold, and F. Aryasetiawan, *Phys. Rev. B* **68**, 233205 (2003).
- [12] M. Guzzo, J. J. Kas, L. Sponza, C. Giorgetti, F. Sottile, D. Pierucci, M. G. Silly, F. Sirotti, J. J. Rehr, and L. Reining, *Phys. Rev. B* **89**, 085425 (2014).
- [13] F. Aryasetiawan, in *Strong Coulomb Correlations in Electronic Structure Calculations*, edited by V. Anisimov (Gordon and Breach Science Publishers, Amsterdam, The Netherlands, 2000), Chap. 1.
- [14] M. Gatti and M. Guzzo, *Phys. Rev. B* **87**, 155147 (2013).
- [15] F. Caruso, H. Lambert, and F. Giustino, *Phys. Rev. Lett.* **114**, 146404 (2015).
- [16] J. S. Zhou, J. J. Kas, L. Sponza, I. Reshetnyak, M. Guzzo, C. Giorgetti, M. Gatti, F. Sottile, J. J. Rehr, and L. Reining, *J. Chem. Phys.* **143**, 184109 (2015).
- [17] J. Lischner, G. K. Pálsson, D. Vigil-Fowler, S. Nemsak, J. Avila, M. C. Asensio, C. S. Fadley, and S. G. Louie, *Phys. Rev. B* **91**, 205113 (2015).
- [18] B. Gumhalter, V. Kovač, F. Caruso, H. Lambert, and F. Giustino, *Phys. Rev. B* **94**, 035103 (2016).

- [19] K. Nakamura, Y. Nohara, Y. Yosimoto, and Y. Nomura, *Phys. Rev. B* **93**, 085124 (2016).
- [20] C. Verdi, F. Caruso, and F. Giustino, *Nat. Commun.* **8**, 15769 (2017).
- [21] D. C. Langreth, *Phys. Rev. B* **1**, 471 (1970).
- [22] J.-J. Chang and D. C. Langreth, *Phys. Rev. B* **5**, 3512 (1972).
- [23] J.-J. Chang and D. C. Langreth, *Phys. Rev. B* **8**, 4638 (1973).
- [24] S. Hüfner, *Photoelectron Spectroscopy: Principles and Applications* (Springer, Berlin, 2003).
- [25] F. De Groot and A. Kotani, *Core Level Spectroscopy of Solids* (CRC Press, Boca Raton, USA, 2008).
- [26] G. D. Mahan, *Phys. Rev.* **145**, 602 (1966).
- [27] D. Dunn, *Can. J. Phys.* **53**, 321 (1975).
- [28] J. L. Skinner, *J. Chem. Phys.* **77**, 3398 (1982).
- [29] D. Hsu and J. L. Skinner, *J. Chem. Phys.* **81**, 1604 (1984).
- [30] G. Mahan, *Many-Particle Physics* (Plenum Press, New York, USA, 1990).
- [31] B. Gumhalter, *Phys. Rev. B* **72**, 165406 (2005).
- [32] P. Lazić, V. M. Silkin, E. V. Chulkov, P. M. Echenique, and B. Gumhalter, *Phys. Rev. Lett.* **97**, 086801 (2006).
- [33] M. Schüler, J. Berakdar, and Y. Pavlyukh, *Phys. Rev. B* **93**, 054303 (2016).
- [34] R. Kubo, *J. Phys. Soc. Jpn.* **17**, 1100 (1962).
- [35] J. J. Kas, J. J. Rehr, and L. Reining, *Phys. Rev. B* **90**, 085112 (2014).
- [36] M. Z. Mayers, M. S. Hybertsen, and D. R. Reichman, *Phys. Rev. B* **94**, 081109 (2016).
- [37] H. Höchst, P. Steiner, and S. Hüfner, *Z. Phys. B: Condens. Matter* **30**, 145 (1978).
- [38] L. Hedin, *J. Phys.: Condens. Matter* **11**, R489 (1999).
- [39] O. Gunnarsson, V. Meden, and K. Schönhammer, *Phys. Rev. B* **50**, 10462 (1994).
- [40] P. Nozières and C. T. De Dominicis, *Phys. Rev.* **178**, 1097 (1969).
- [41] L. Hedin, *Phys. Scr.* **21**, 477 (1980).
- [42] C.-O. Almbladh and L. Hedin, in *Handbook on Synchrotron Radiation*, edited by E. E. Koch (North Holland Pub. Co., Amsterdam, Netherlands, 1983), Vol. 1, Chap. 8.
- [43] M. Gatti, G. Panaccione, and L. Reining, *Phys. Rev. Lett.* **114**, 116402 (2015).
- [44] F. Bruneval and M. Gatti, *Top. Curr. Chem.* **347**, 99 (2014).
- [45] G. Stefanucci, Y. Pavlyukh, A.-M. Uimonen, and R. van Leeuwen, *Phys. Rev. B* **90**, 115134 (2014).
- [46] J. S. Zhou, Ph.D. thesis, Ecole Polytechnique, Université Paris-Saclay, France, 2016.
- [47] W. Schülke, *Electron Dynamics by Inelastic X-Ray Scattering*, Oxford Series on Synchrotron Radiation (Oxford University Press, Oxford, 2007).
- [48] E. Runge and E. K. U. Gross, *Phys. Rev. Lett.* **52**, 997 (1984).
- [49] C. Ullrich, *Time-Dependent Density-Functional Theory: Concepts and Applications*, Oxford Graduate Texts (Oxford University Press, Oxford, 2012).
- [50] A. Zangwill and P. Soven, *Phys. Rev. A* **21**, 1561 (1980).
- [51] M. Petersilka, U. J. Gossmann, and E. K. U. Gross, *Phys. Rev. Lett.* **76**, 1212 (1996).
- [52] G. Onida, L. Reining, and A. Rubio, *Rev. Mod. Phys.* **74**, 601 (2002).
- [53] S. Botti, A. Schindlmayr, R. D. Sole, and L. Reining, *Rep. Prog. Phys.* **70**, 357 (2007).
- [54] B. Holm and F. Aryasetiawan, *Phys. Rev. B* **56**, 12825 (1997).
- [55] F. Caruso and F. Giustino, *Eur. Phys. J. B* **89**, 238 (2016).
- [56] D. Vigil-Fowler, S. G. Louie, and J. Lischner, *Phys. Rev. B* **93**, 235446 (2016).
- [57] M. Cazzaniga, H.-C. Weissker, S. Huotari, T. Pylkkänen, P. Salvestrini, G. Monaco, G. Onida, and L. Reining, *Phys. Rev. B* **84**, 075109 (2011).
- [58] R. Wyckoff, *Crystal Structures*, Vol. 1 (Interscience Publishers, New York, 1963), 2nd ed.
- [59] M. Taut, *J. Phys. C* **20**, 2961 (1987).
- [60] K. Sturm, E. Zaremba, and K. Nuroh, *Phys. Rev. B* **42**, 6973 (1990).
- [61] A. A. Quong and A. G. Eguiluz, *Phys. Rev. Lett.* **70**, 3955 (1993).
- [62] M. Gatti, I. V. Tokatly, and A. Rubio, *Phys. Rev. Lett.* **104**, 216404 (2010).
- [63] V. M. Silkin, P. Lazić, N. Došlić, H. Petek, and B. Gumhalter, *Phys. Rev. B* **92**, 155405 (2015).
- [64] J. E. Northrup, M. S. Hybertsen, and S. G. Louie, *Phys. Rev. Lett.* **59**, 819 (1987).
- [65] J. E. Northrup, M. S. Hybertsen, and S. G. Louie, *Phys. Rev. B* **39**, 8198 (1989).
- [66] M. Cazzaniga, *Phys. Rev. B* **86**, 035120 (2012).
- [67] J. Lischner, T. Bazhiron, A. H. MacDonald, M. L. Cohen, and S. G. Louie, *Phys. Rev. B* **89**, 081108 (2014).
- [68] E. Jensen and E. W. Plummer, *Phys. Rev. Lett.* **55**, 1912 (1985).
- [69] I.-W. Lyo and E. W. Plummer, *Phys. Rev. Lett.* **60**, 1558 (1988).
- [70] A. W. Overhauser, *Phys. Rev. Lett.* **58**, 959 (1987).
- [71] Kenneth W.-K. Shung and G. D. Mahan, *Phys. Rev. Lett.* **58**, 960 (1987).
- [72] A. W. Overhauser, *Phys. Rev. Lett.* **55**, 1916 (1985).
- [73] Kenneth W.-K. Shung and G. D. Mahan, *Phys. Rev. Lett.* **57**, 1076 (1986).
- [74] Kenneth W.-K. Shung, B. E. Sernelius, and G. D. Mahan, *Phys. Rev. B* **36**, 4499 (1987).
- [75] G. Mahan and E. Plummer, *Handbook of Surface Science* **2**, 953 (2000).
- [76] W. Bardyszewski and L. Hedin, *Phys. Scr.* **32**, 439 (1985).
- [77] L. Hedin, J. Michiels, and J. Inglesfield, *Phys. Rev. B* **58**, 15565 (1998).
- [78] D. A. Shirley, *Phys. Rev. B* **5**, 4709 (1972).
- [79] N. Troullier and J. L. Martins, *Phys. Rev. B* **43**, 993 (1991).
- [80] X. Gonze, G.-M. Rignanese, M. Verstraete, J.-M. Beuken, Y. Pouillon, R. Caracas, F. Jollet, M. Torrent, G. Zerah, M. Mikami *et al.*, *Z. Kristallogr.* **220**, 558 (2005).
- [81] M. van Schilfgaarde, T. Kotani, and S. Faleev, *Phys. Rev. Lett.* **96**, 226402 (2006).
- [82] M. Cazzaniga, L. Caramella, N. Manini, and G. Onida, *Phys. Rev. B* **82**, 035104 (2010).
- [83] J. S. Zhou *et al.* (unpublished).
- [84] M. Trzhaszkovskaya, V. Nefedov, and V. Yarzhemsky, *At. Data Nucl. Data Tables* **77**, 97 (2001).
- [85] The inclusion of the photoionization cross sections following [6] was not possible here on the basis of available atomic data [84] as in the Na atom the  $3p$  shell is completely empty, contrary to the bulk case.
- [86] The non-noticeable difference stems from the fact that in Ref. [16] the TOC was calculated based on a multipole sampling of  $\text{Im } \Sigma_{xc}$ , while in this paper all the CEA results are produced using a new cumulant code based on a numerical integration of Eqs. (8) and (9) [83].